Numerical investigation of hydraulic instability of pump-turbines in fast pump-to-turbine transition

Numerical investigation of hydraulic instability of pump-turbines in fast pump-to-turbine transition

Xiaotong Yan[a], Fei Zhang[b], Yuan Zheng[a,c], Kan Kan[a,c,*], Mosè Rossi[d]

[a]College of Water Conservancy and Hydropower Engineering, Hohai University, Nanjing, 210098, PR China

[b]Pumped Storage Technological & Economic Research Institute of State Grid Xinyuan Company Ltd., Beijing, 100761, China

[c]College of Energy and Electrical Engineering, Hohai University, Nanjing, 211100, PR China

[d]Department of Industrial Engineering and Mathematical Sciences (DIISM), Marche Polytechnic University, Ancona, 60131, Italy

*Correspondence: kankan@hhu.edu.cn; Tel.: +86 15151862390

Abstract: The fast pump-to-turbine transition of a pumped storage unit is highly responsive to electrical power system regulation demands and is a critical process for the unit itself. The correct prediction of this hydraulic transient process is crucial to avoid issues during machine operation. In this study, a three-dimensional numerical model of the transition process of a pumped storage hydraulic system was proposed and analyzed. Numerical simulations were performed to investigate the variations in external parameters, pressure pulsations, and the evolution of internal flow patterns and vortical structures in the pump turbine. The results showed that the stepwise variations in the flow rate, torque, and force were synchronized with the movement of the guide vanes. Notably, during the pump braking operation and runner speed reversal, a considerable time period with significant force oscillations and intense torque fluctuations occurred, particularly in the vaneless region, where pressure fluctuations were notable. Vortical structures that induce vibrations and intense pressure fluctuations were localized near the runner inlet and at the leading and trailing edges of the guide and stay vanes. This study offers theoretical insights that are crucial for enhancing the stability of the fast pump-to-turbine transitional process, thus optimizing its control strategies.

Keywords: Numerical investigation; Pumped storage; Pump-turbine; Fast pump-to-turbine; Hydraulic instabilities

Nomenclature

n_r	Runner rated speed (rad/s)
k	Turbulence kinetic energy (m^2/s^2)
ω	Specific dissipation rate (m^2/s^2)
t	Physical time (s)
u_j	Velocity component (m/s)
x_j	Cartesian coordinate component (m)
P_k	Turbulence production due to viscous forces (m^2/s^3)

v	Kinematic viscosity (m^2/s)
v_t	Eddy viscosity (m^2/s)
S	Invariant measure of the strain rate (s^{-1})
r	Grid refinement ratio
h_{coarse}	Size of the coarse grid
h_{fine}	Size of the fine grid
Q	Flow rate (m^3/s)
η	Efficiency (%)
n_t	Runner speed (r/s)
M	Torque (N·m)
J	Rotational inertia (kg·m^2)
∇t	Time step (s)
γ_{t}	Angular velocity (r/s)
H	Head (m)
$\boldsymbol{\bar{\omega}_{Ri}}$	Reynolds-averaged rigid vorticity component (s^{-1})
$\boldsymbol{\bar{\omega}_{Si}}$	Reynolds-averaged shear vorticity component (s^{-1})
$\boldsymbol{\bar{\omega}_{i}}$	Reynolds-averaged vorticity component (s^{-1})
$\boldsymbol{\bar{c}_{i}}$	Angular velocity component of the rotating system (rad/s)
$\boldsymbol{\bar{u}_{ri}}$	Relative velocity component (m/s)
E_v	Evolution intensity of the enstrophy for the unit volume (s^{-3}/m^3)
Ω_R	Enstrophy of the rigid vorticity (s^{-2})

Abbreviations

ASME	American Society of Mechanical Engineers
ECFT	Enstrophy of the Coriolis Force Term
ERCT	Enstrophy of the Pseudo Lamb Vector Curl Term
ERDT	Enstrophy of the Rigid Vorticity Dilatation Term
ERST	Enstrophy of the Rigid Vorticity Stretching Term
ERRT	Enstrophy of the Reynolds Stress Term
ERVT	Enstrophy of the Viscous Term
GCI	Grid Convergence Index
GVO	Guide Vane Opening
RANS	Reynolds-Averaged Navier-Stokes
URANS	Unsteady Reynolds-Averaged Navier-Stokes
RSM	Reynolds Stress Model
SIMPLEC	Semi-Implicit Method for Pressure-Linked Equations-Consistent
SST	Shear Stress Transport
UDF	User Defined Function

1 Introduction

Widespread adoption of renewables is essential for achieving the environmental target of net-zero carbon emissions by 2050 [1]. In this context, hydropower has emerged as a highly promising solution for significantly boosting power generation capability and providing energy storage capacity. Pumped storage stations are among the most mature and efficient mechanical storage technologies [2]. Indeed, they fulfill several roles, such as peak shaving, valley filling, frequency and phase regulation, and standby capabilities, in the case of emergencies. Considering the prevailing trend towards the gradual integration of large-scale renewable energy into the power grid, pumped storage stations can play a pivotal role in counteracting the intermittency and instability associated with renewable energy sources, thus ensuring the safe and stable operation of modern power systems [3].

To align with the dynamic service demands of power systems, pumped storage stations often exhibit distinctive features such as multipurpose operation, rapid mode transitions, frequent start-stop cycles, and heightened pressure pulsations. Consequently, these characteristics increase complex hydraulic transient issues in the water-conveyance system [4-7]. Several researchers have conducted extensive numerical simulations and studies to explore various transition processes within pump turbines. Liu et al. [8] performed numerical simulations of the transient power failure process of a prototype pump turbine. The results showed that the reverse flow in the casing and vane, as well as the stall phenomenon in the runner, led to a smooth change in the head when the flow rate was close to zero, whereas it became evident when the flow rate increased. In particular, the stall phenomenon considerably influenced the pressure distribution on the runner surface. Li et al. [9] performed numerical simulations of a prototype pump turbine during a normal shutdown process. The results showed a concurrent decrease in the flow rate and torque, along with a reduction in the rotational speed, owing to the negative torque applied to the runner as the guide vanes close. They proposed an approach for predicting the transient characteristics of a pump turbine during the shutdown process, and provided details on its internal fluid dynamic behavior. Zhang et al. [10] developed a dynamic model for simulating pump-turbine operation in S-shaped regions under runaway conditions. They introduced dynamic relative parameters along with a dynamic nonlinear model of the pump turbine, thus providing a new perspective for modeling transient processes in pump turbines. Consequently, a good match between the dynamic model and theoretical analysis was obtained, thus validating the proposed model. Regarding the load rejection in a pump-turbine, Mao et al. [11] explored the application of a co-adjusting inlet valve and guide vane method to enhance the internal fluid stability. They combined a theoretical analysis with a numerical simulation, and the results showed that the proposed method was beneficial to the operational stability of the entire system. Jin et al. [12] simulated the start-up process of the turbine mode to pinpoint the precise location of the flow energy dissipation within the pump turbine. The trailing edge of the guide vane had both high flow energy dissipation and turbulence kinetic energy values, whereas the wall shear stress and axial and radial forces had a significant effect on the fluid flow characteristics.

Using hydraulic braking to accelerate the transition from pump operation to turbine operation, the fast pump-to-turbine transition process in pumped storage stations is one of the most intricate and hazardous operating zones that involves complex hydraulic, mechanical, and electrical processes [13]. Modern power systems require enhanced rapid response times from pumping to power generation, thus requiring swift transitions. In contrast to the conventional transition mode involving electrical and mechanical braking, the use of hydraulic braking to accelerate the pump shutdown introduces additional complexity into the transition process. Current research on the transition processes of pumped-storage stations has primarily focused on load-rejection, shutdown, startup, and runaway processes without providing insights into the intricate hydraulic variations in the fast pump-to-turbine transition process [14-17]. To the best of our knowledge, this hydraulic change has hampered the formulation of accurate and effective control strategies for the transition process.

This study presents a three-dimensional numerical model of the entire flow system of a pumped storage station operating during a fast pump-to-turbine transition process. The changes in runner speed, flow rate, torque, and force characteristics under a specified control strategy were investigated. The study also explored the duration to complete the transition and examined the pressure pulsations in the pump turbine during the rapid transition. Furthermore, the evolution of the flow patterns and vortical structures was analyzed. This study provides crucial references for reducing the time required for operational state transitions and enhancing station responsiveness to the power grid. It also offers theoretical support for improving stability and optimizing control strategies during the fast pump-to-turbine transition process.

The paper is structured as follows: Section 2 presents the numerical simulation model along with the numerical settings and details of the numerical grid with its independence study. Section 3 describes the fast pump-to-turbine transition process and its hydraulic transient mechanism from various perspectives, including external parameter changes, pressure pulsations, flow patterns, and vortical structure evolution. Finally, Section 4 reports the main research findings and future developments of this study.

2 Numerical considerations

2.1 Computational model and grid

The computational model of the entire flow system of the pumped storage station analyzed in this study is shown in Fig. 1, with a Guide Vane Opening (GVO) of 22° (rated operating conditions). The computational domain embedded an upstream penstock, a mixed-flow pump-turbine unit, and a downstream penstock. The computational domain of the pump-turbine unit was divided into the spiral casing, stay vanes (20 vanes), guide vanes (20 vanes), runner (9 vanes), and draft tube. The essential parameters of both the power station and the pump-turbine unit are listed in Table 1.

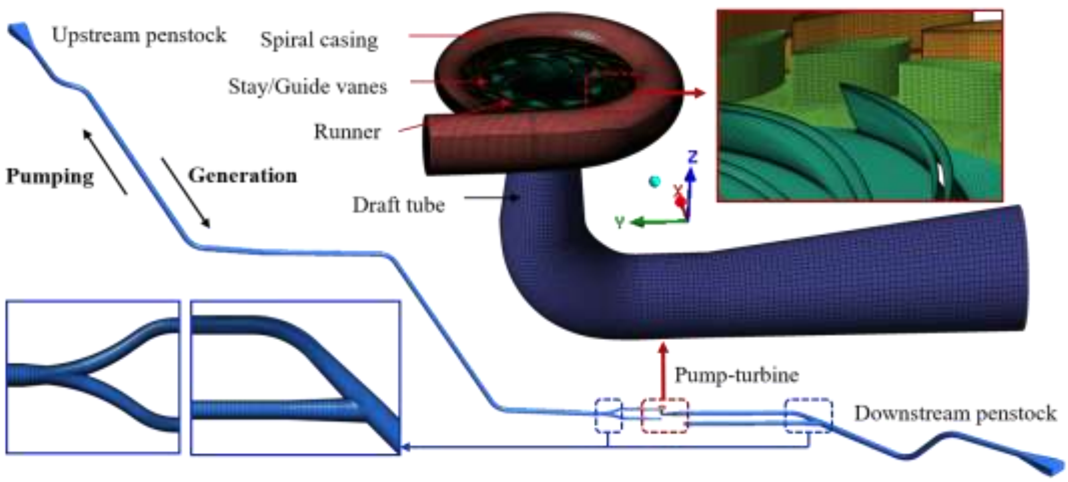

Figure 1. Computational domain and grid of the pumped storage power station

Table 1. Main geometric parameters of the pumped storage power station

Parameter	Value
Upstream reservoir normal storage level (m)	716
Downstream reservoir normal storage level (m)	299
Type of pump-turbine	HLNA1518-LJ-412
Rated output power in turbine mode (MW)	306.1
Maximum input power in pump mode (MW)	≤325
Rated rotational speed n_r (rad/s)	44.88
Moment of inertia of the generator ($t \cdot m^2$)	6000
Moment of inertia of the pump-turbine ($t \cdot m^2$)	240
Elevation of guide vane centerline (m)	192

Hexahedrally structured grids were used in the upstream penstock, spiral casing domain, stay vane domain, runner domain, draft tube domain, and downstream penstock to control the overall grid node count. In the guide vane domain, a prism grid was generated using the dynamic mesh method to simulate guide vane closure or opening. Two-dimensional refined quad and triangular meshes were generated in the boundary layer regions and main-flow region of the guide vane bottom side. Subsequently, the two-dimensional mesh on the bottom side of the guide vane was extruded to the top side of the guide vane using a copper meshing operation in Gambit. Specifically, grid generation for the runner domain was performed using ANSYS-TurboGrid software. The grids for the remaining computational domains were created using ANSYS-ICEM software. For the pump-rated operating conditions, the y + values of the runner blades were maintained in close proximity to 30. Since these y+ values are compatible with the Shear Stress Transport k-ω (SST k-ω) turbulence model, they were selected by examination of the ANSYS software manual and other research studies in the scientific literature located in [18]. Because it uses an autonomous wall function to consider near-wall flow features, this model is regarded as one of the best for analyzing a number of issues related to the study of the transition process in hydraulic turbines. This enables a good compromise between simulation timing and accuracy [19].

2.2 Governing equations and numerical settings

ANSYS Fluent 2022R1 software was used to perform the numerical simulations. As previously mentioned, the SST k-ω turbulence model has been selected to close the control equations, providing a dual-equation eddy-viscosity model that integrates the advantages of the standard k-ε and k-ω turbulence models [20, 21]. It can be described as the k and ω equations:

$$\frac{\partial k}{\partial t}+\frac{\partial\left(u_j k\right)}{\partial x_j}=P_k-\beta^* k\omega+\frac{\partial}{\partial x_j}\left[\left(\nu+\sigma_k\nu_t\right)\frac{\partial k}{\partial x_j}\right] \tag{1}$$

$$\frac{\partial \omega}{\partial t}+\frac{\partial\left(u_j \omega\right)}{\partial x_j}=\gamma S^2-\beta\omega^2+\frac{\partial}{\partial x_j}\left[\left(\nu_t+\sigma_\omega\nu_t\right)\frac{\partial \omega}{\partial x_j}\right]+2\left(1-F_1\right)\frac{\sigma_{\omega 2}}{\omega}\frac{\partial k\partial\omega}{\partial x_j\partial x_j} \tag{2}$$

where k denotes the turbulence kinetic energy, m^2/s^2; ω denotes the specific dissipation rate, m^2/s^2; t

denotes time, s; u_j (j=1, 2, 3) represents the velocity component, m/s; x_j (j=1, 2, 3) represents the Cartesian coordinate component, m； P_k denotes the turbulence production due to viscous forces, m^2/s^3; v denotes kinematic viscosity, m^2/s; v_t denotes eddy viscosity, m^2/s; S denotes the invariant measure of the strain rate, s^{-1}. All coefficients for this model are obtained by functions of $\varphi = \varphi_1 F_1 + \varphi_2 (1- F_1)$. The constants are as follows: β^* =0.09, β_1 =0.075, β_2 =0.0828, σ_{k1} =0.85, σ_{k2} =1, γ_1 =0.556, γ_2 =0.44, $\sigma_{\omega 1}$ =0.5, $\sigma_{\omega 2}$ =0.856.

For transient simulations using unsteady Reynolds-averaged Navier (URANS) equations, the initial conditions were derived from steady-state simulations. Both steady-state and transient computations used the Semi-Implicit Method for Pressure-Linked Equations-Consistent (SIMPLEC) algorithm for the coupled solution of the velocity and pressure equations. Convective and diffusive terms were discretized using a second-order upwind scheme, and time discretization employed a first-order implicit format. The results of steady-state simulations act as the initial flow field for transient simulations, with a specified transient simulation time step of $1.17 \cdot 10^{-3}$ s that corresponds to a 3° rotation of the runner at the rated rotational speed. The convergence criterion for the residual of the Reynolds Stress Model (RSM) at each time step is set to 10^{-5}. Additionally, the gravitational acceleration was defined as g = 9.81 m/s^2.

In the entire flow-domain system model, the downstream inlet exhibits a pressure inlet boundary condition, whereas the upstream outlet exhibits a pressure outlet boundary condition. The reservoir depths are calculated based on the actual water levels downstream and upstream, and the pressure values for the downstream inlet and upstream outlet are set to 426,330.76 Pa and 836,199.15 Pa, respectively.

2.3 Grid independence study

The Richardson extrapolation method was applied in this investigation to verify grid independence using the Grid Convergence Index (GCI) for a quantitative evaluation of the computational results [22-25]. The three grid partitioning strategies used for the convergence analysis are identical, involving a reduction in both grid quantity and scale. According to the recommendations of the American Society of Mechanical Engineers (ASME), the refinement ratio $\boldsymbol{r}$ should exceed 1.3 for grid refinement [26], which is defined by Eq. (3), where h_{coarse} represents the coarse grid size and h_{fine} represents the fine grid size, respectively. Consequently, the quantities of the three sets of grids are 20.43 million, 8.62 million, and 3.88 million, respectively.

$$r = \frac{h_{\text{coarse}}}{h_{\text{fine}}}, h = \left[\frac{1}{N} \sum_{i=1}^{N} \left(\Delta V_i \right) \right]^{1/3} \tag{3}$$

Table 2. Quantities of three sets of grids

Computational domain	Number of nodes in S1 (10^5)	Number of nodes in S2 (10^5)	Number of nodes in S3 (10^5)
Upstream penstock	15.66	6.46	2.34
Spiral casing	24.79	11.19	4.87
Stay vanes	29.41	12.41	5.72
Guide vanes	27.92	11.58	5.13
Runner	68.85	28.73	13.54

Draft tube	28.34	12.07	5.43
Downstream penstock	9.37	3.72	1.78
Sum	204.34	86.16	38.81

Numerical simulations of all grid sets were performed under the rated conditions of the pump mode, considering the flow rate and efficiency as variables for the convergence analysis. Table 3 lists the results of the grid independence study, showing convergence indices for the flow rate and efficiency of 2.53% and 1.35%, respectively. These values confirmed that the grids satisfied the convergence criterion (less than 3%) [27]. Considering both the simulation accuracy and computational costs, a computational grid with 8.62 million elements was chosen for performing all numerical simulations.

Table 3. Grid independence study

Parameter	$\varphi=Q$ (m^3/s)	$\varphi=\eta$ (%)
N_1	20,428,557	
N_2	8,624,839	
N_3	3,880,253	
Mesh refinement factor r_{21}	1.33	
Mesh refinement factor r_{32}	1.31	
Numerical value φ_1	60.47	93.14
Numerical value φ_2	60.18	93.02
Numerical value φ_3	54.47	91.72
Apparent order p	11.1541	8.8932
Extrapolated value φ_{ext}^{21}	60.482	93.15
Relative error e_a^{21}	0.480%	0.129%
Extrapolated error e_{ext}^{21}	0.020%	0.011%
Grid convergence index GCI_{fine}^{21}	2.53%	1.35%

2.4 Control method of varying the angular speed

The fast pump-to-turbine transition process significantly reduces the transition time compared with the normal pump-to-turbine transition process, thus enhancing the responsiveness of the pumped-storage station to power system demands. The main distinction occurs in the normal transition when a spherical valve undergoes a "fully open→fully closed→fully open" process, using a combination of electrical and mechanical braking. In contrast, during the rapid transition, the spherical valve remained stationary, and a rapid shutdown was achieved through hydraulic braking.

The control process for the fast pump-to-turbine is as follows: Upon receiving the transition command, the unit closes the guide vanes to reduce the pump input. Once the guide vanes were fully closed, the electric motor circuit breaker was disconnected, the system was demagnetized, and the unit speed began to decrease. When the speed decreased to approximately 50% of the rated speed, the guide vanes were preopened for hydraulic braking. As the speed reversed and entered turbine mode, reaching approximately 50% of the rated rotational speed, the guide vanes were further opened to the no-load position, ultimately transitioning the unit to the turbine no-load operating condition.

The algorithmic implementation of the control strategy in this study is outlined as follows. The speed of the runner changes with time according to the angular momentum equation shown in Eq. (4). During the transient simulations, the torque acting on the runner blades was monitored at each time step, and the runner speed for the next time step was predicted using Eq. (4).

$$n_t = \begin{cases} n_r \left(t \le 26\text{s}\right) \\ n_{t-\Delta t} + \dfrac{30}{\pi}\dfrac{M}{J} \times \Delta t\left(t > 26\text{s}\right) \end{cases} , \tag{4}$$

where M is the total torque of the runner, N·m; J is the total rotational inertia of runner and generator,kg·m^2; t is the time, s; Δt is the time step, s.

The motion of the guide vanes is described by Eq. (5) and shown in Fig. 3, where γ_t represents the angular velocity of the guide vanes at time t in r/s. To simulate the motion process of the guide vanes, dynamic mesh techniques were used in this study, with a combination of elastic smoothing and a 2.5D remeshing algorithm. It is worth noting that, in practical computations, as the opening of the guide vanes approaches 0°, the grid quality in the guide vane region deteriorates sharply. To ensure smooth calculations, the opening of the guide vanes was maintained at 0.5° between 26s - 45.36s.

$$\gamma_t = \begin{cases} 0\left(t \le 10\text{s}\right) \\ \text{-}0.0234528625\left(10\text{s}<t \le 26\text{s}\right) \\ 0\left(26\text{s} < t \le 45.36\text{s}\right) \\ 0.00872665\left(45.36\text{s} < t \le 50.36\text{s}\right) \\ 0\left(50.36\text{s} < t \le 80.88\text{s}\right) \\ 0.00872665\left(80.88\text{s} < t \le 87.88\text{s},\right) \\ 0\left(\text{t} > 87.88\text{s}\right) \end{cases} \tag{5}$$

By implementing a user-defined function (UDF) program within ANSYS Fluent 2022R1, Eq. (4) dynamically modulates the runner’s rotational speed, and Eq. (5) simulates the motion of guide vanes. The UDF allows the system to dynamically adjust the simulation parameters in real-time, thus aligning with the fast pump-to-turbine transition process control strategy. This approach accurately replicates the dynamic responses of an actual system runner and guide vanes.

3 Results and Discussion

3.1 Validation of the numerical results

Fig. 2 shows the experimental and numerical results of the pump-turbine performance in both pump and turbine modes at various guide vane openings. The numerical simulations revealed good agreement with the experimental results. In the pump mode, the maximum relative error percentage difference in the head and efficiency was always below 5%. Similarly, in the turbine mode, the relative error percentage difference in the head and efficiency was always below 4.61%.

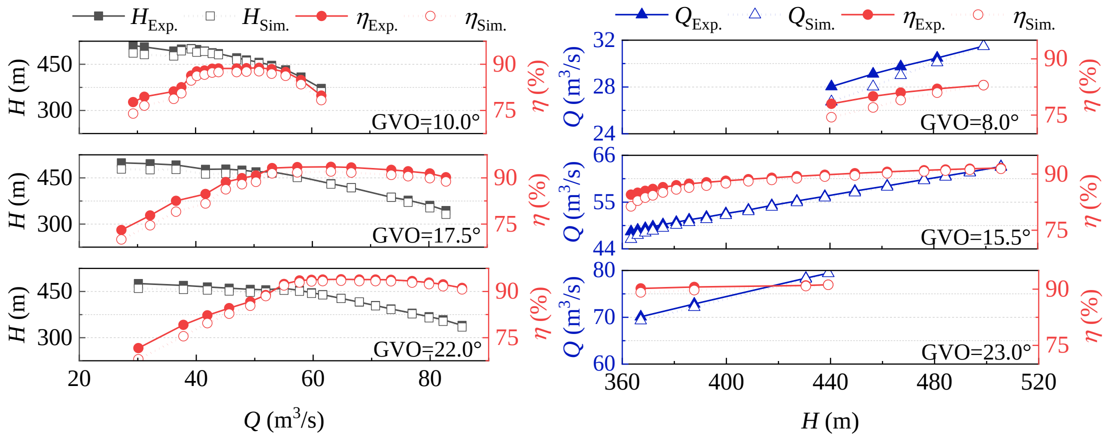

(a) Pump mode

(b) Turbine mode

Figure 2. Experimental vs. numerical results of the pump-turbine performance in both pump and turbine modes

3.2 Time histories of external parameters during the fast pump-to-turbine transition process

The control strategy and variations in the rotational speed and flow rate during the fast pump-to-turbine transition process of the pumped storage system are shown in Fig. 3. Initially, the unit operated under a stable rated condition in the pump with the guide vane opening set at 22° (relative opening of 100%). After 10 s, the unit received a transition command that started the gradual closure of the guide vanes and the subsequent reduction in the flow rate. After 26 s, the guide vanes completed their closure (relative opening of 2.3%) and the circuit breaker of the electric motor was disconnected, resulting in demagnetization. Consequently, the runner's rotational speed decreases, leading to a continuous decrease in the flow rate. At 35.2 s, the instantaneous flow rate drops to zero and marks the commencement of the flow reversal in the turbine-mode direction. At 45.36 s, the guide vanes initiate a pre-opening to 3° (relative opening of 13.6%) for hydraulic braking. At 66.7 s, the runner's instantaneous rotational speed drops to zero and initiates a reverse rotation in the turbine mode. At 80.88 s, the guide vanes began to open further to a no-load opening of 6.5° (a relative opening of 29.5%). After 119.5 s, the unit enters a stable turbine no-load operating condition and completes the transition process at 109.5 s.

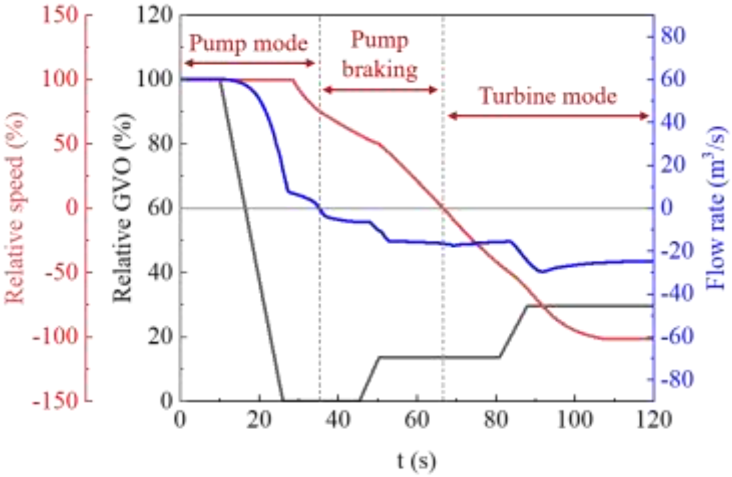

Figure 3. Control strategy and time histories of speed and flow rate

From the initial moment until 35.2 s, the pump-turbine unit operated in pump mode. From 35.2 to 66.7 s, the pump-turbine unit undergoes pump braking that accelerates the pump shutdown under the influence of hydraulic braking. After 66.7 s, the pump-turbine unit started to operate in the turbine mode. The schematic diagrams of the three operational modes of the pump-turbine are shown in Fig. 4.

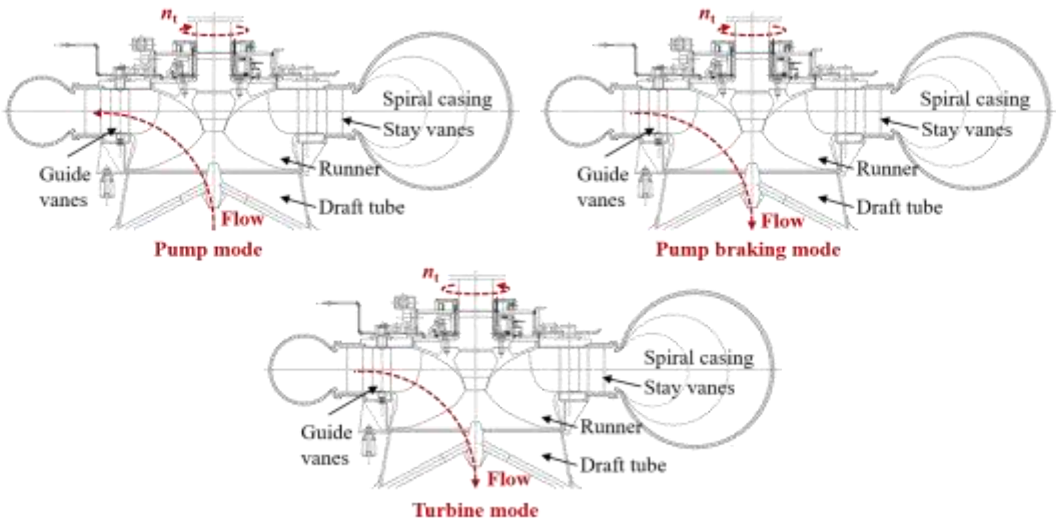

Figure 4. Schematic diagram of different operating modes of pump-turbine

The torque and force variations during the fast pump-to-turbine transition process in the pumped-storage system are shown in Fig. 5. The torque and force experienced by the runner were primarily influenced by the combined effects of the unit flow rate and runner speed. During the pump shutdown, the torque decreased steadily. Upon entering the pump-braking operating conditions and activating the guide vanes for hydraulic braking, the torque on the blades increased and exhibited significant fluctuations. Once the unit has started its operation in the turbine mode and the guide vanes are opened to the no-load position, the blade torque consistently decreases to the null value.

Positive axial forces were present during the reversal of the runner's rotational direction. The combined action of the X- and Y-axis radial forces is reflected in the oscillation direction and the intensity of the unit in the horizontal plane (the definitions of the X- and Y-axis directions are shown in Fig. 1). It is evident that under the pump-braking operating condition, the unit experiences more pronounced oscillations when the guide vanes move.

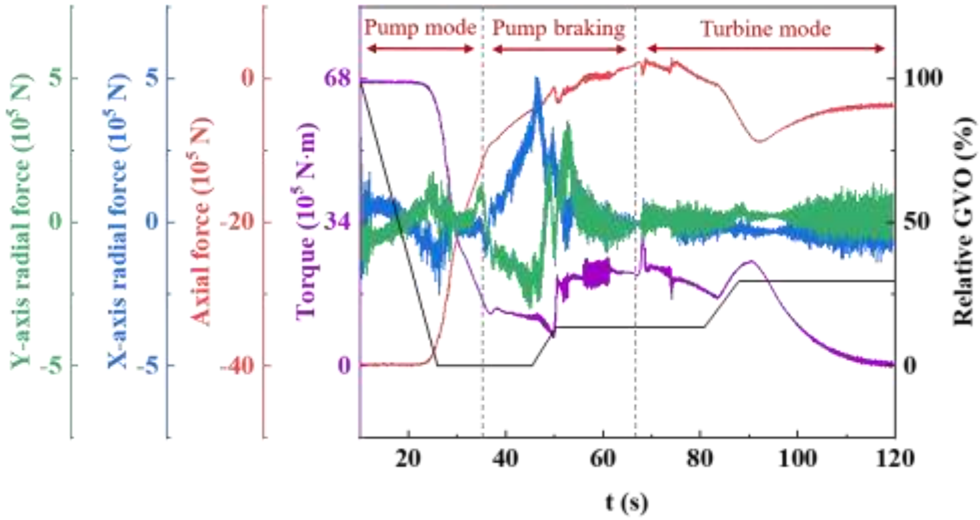

Figure 5. Time histories of torque and force

3.3 Pressure fluctuations during the fast pump-to-turbine transition process

To investigate the pressure fluctuations during the fast pump-to-turbine transition process in the pump-turbine system, eight monitoring points were strategically placed within the pump-to-turbine unit, as shown in Fig. 6. P-SC1 is located in the spiral casing region near the upstream penstock; P-SC2 is placed in the spiral casing region near the stay vanes; P-SV1 is situated in the stay vane region; P-GV1 is positioned in the guide vane region; P-VL1 is placed in the vaneless region between the guide vanes and the runner; P-RN1 is located in the runner region; P-DT1 is situated in the draft tube region near the interface between the runner and the draft tube; and P-DT2 is positioned within the elbow section of the draft tube region on the inner side. Fig. 6 provides a graphical overview of the setup of the monitoring points described thus far.

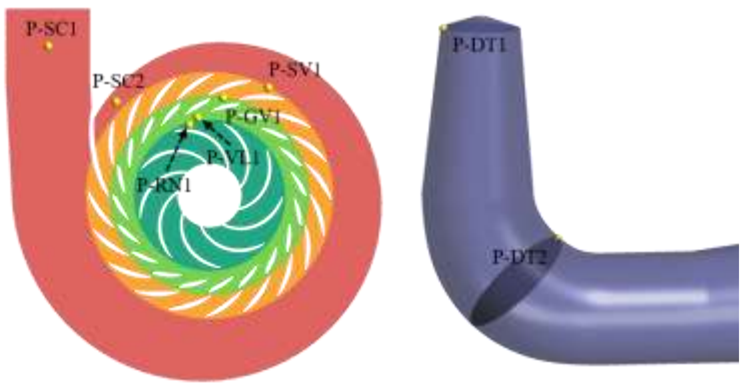

Figure 6. Schematic of monitoring points

The pressure fluctuations at each monitoring point during the fast pump-to-turbine transition are shown in Fig. 7. Monitoring points P-SC1, P-SC2, P-SV1, and P-GV1 showed similar trends in temporal pressure variation. However, the magnitude of the pressure change increased from the spiral casing region to the guide vanes. Using the guide vanes as a boundary, during the fast pump-to-turbine transition process, when the guide vanes are closed, there is a rapid decrease in the pressure in the spiral casing and stay vane regions. The inertia of the water flow led to a sudden pressure increase in the runner and draft tube regions.

The pressure variations in the vaneless and runner regions exhibited similar trends. During pump braking, under the influence of vortical structures at different scales and intensities, there was a significant intensification of pressure fluctuations in both the vaneless and runner regions, with the most pronounced fluctuations observed in the former. The pressure changes in the draft tube region at the two monitoring points were nearly identical (P-DT1 and P-DT2 in Fig. 6), indicating that the pressure in the straight cone section of the draft tube did not exhibit significant variations. No evident phenomena, such as the formation of a tailrace eddy, caused intense pressure pulsations within the draft tube.

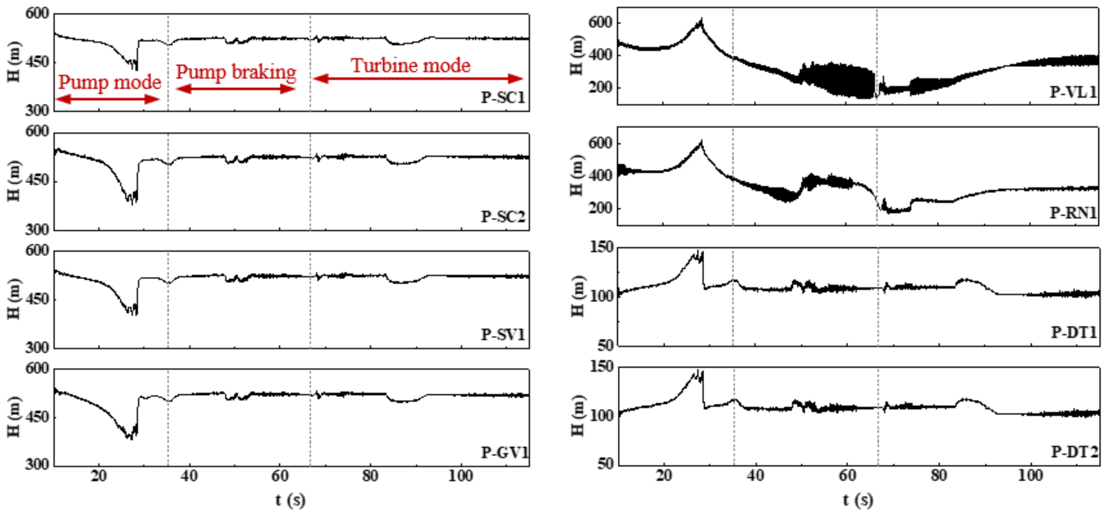

Figure 7. Time histories of pressure fluctuations at different monitoring points

3.4 Evolution of flow patterns and vortical structures during the fast pump-to-turbine transition process

3.4.1 Selection of transition process characteristic moments

To further explore the variations in the internal factors influencing the runner force during the fast pump-to-turbine transition process, a detailed study and analysis of the evolution of the internal flow field of the pump-turbine unit were conducted. Six representative moments were selected for an in-depth analysis as follows:

t_1=10.0 s: initial pump operating condition; t_2=26.0 s: onset of runner rotational speed decrease; t_3=35.2 s: zero flow rate within the pump-turbine unit; t_4=66.7 s: runner rotational speed reaches zero; t_5=83.5 s:

runner rotational speed rises to 50% of the rated speed in turbine mode. Blade torque continuously decreases and leads to the onset of turbine no-load conditions; and t_6=119.5 s: stable turbine no-load operating conditions.

3.4.2 Identification and distribution of vortical structures

During the fast pump-to-turbine transition process in pumped storage, unstable flow structures are predominantly concentrated in the stay vanes, guide vanes, and runner regions. Employing the rigid vorticity-based vortex identification method, as well as the improvements made in this area by other scientists [28–32], has been shown to be reliable and may prevent significant shear mixing compared to other vortex identification methods [33-37]. With a rigid vorticity amplitude of 120 s^{-1}, as an isosurface colored by turbulent kinetic energy, the distribution of vortical structures at the six characteristic moments is shown in Fig. 8.

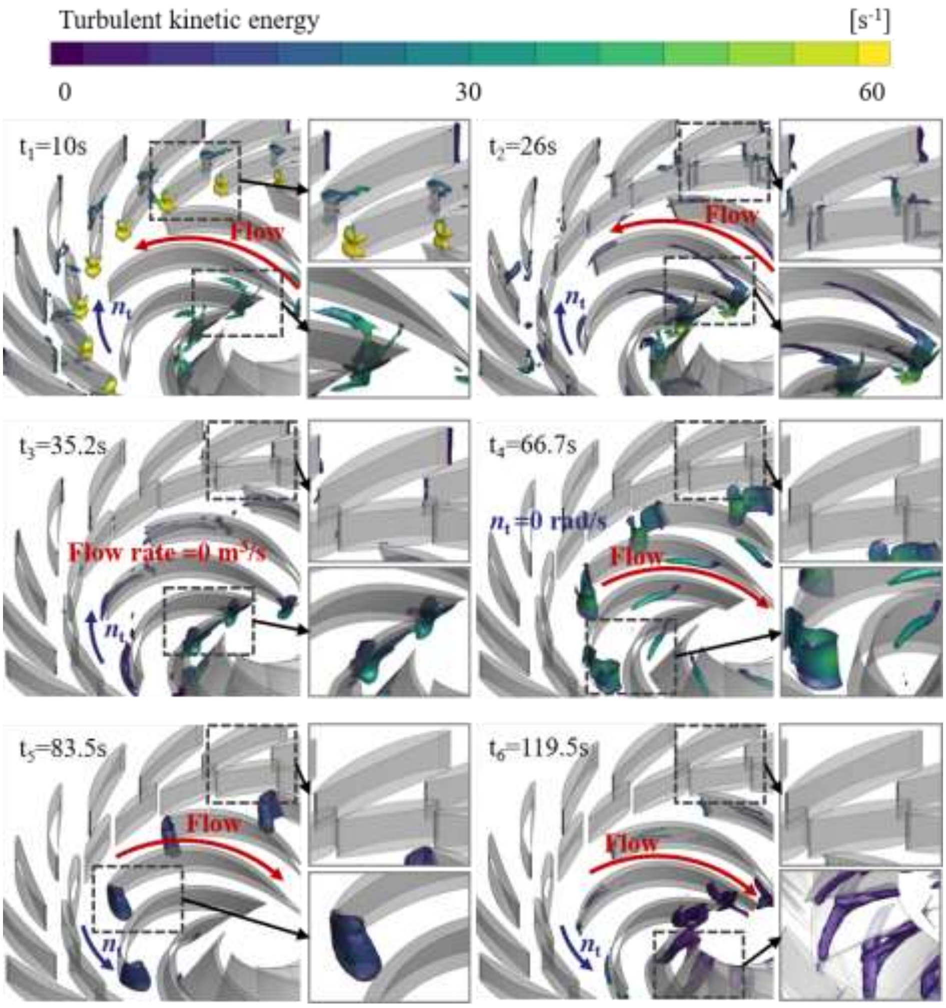

Figure 8. Vortical structures during the fast pump-to-turbine transition process (Rigid vorticity =120 s^{-1}, colored by turbulent kinetic energy)

In the initial pump operating condition, vortical structures were primarily distributed near the runner inlet and leading edges of the guide and stay vanes under the impact of the water flow. The results indicate that the flow field at the leading edges of the guide vanes has high turbulent kinetic energy, which means that a high energy dissipation will be generated owing to the high flow rate and strong impact of the water flow on the leading edges of the guide vanes under this condition. Regardless of whether the unit is operating in pump or turbine mode, vortical structures in the runner domain consistently appear near the runner inlet.

In pump mode, vortical structures are likely to occur at the leading and trailing edges of both the guide and stay vanes. In turbine mode, vortical structures in the guide and stay vane regions primarily manifest at the trailing edges of the vanes. In addition, the turbulent kinetic energy dissipation in the turbine mode was correspondingly reduced owing to the lower flow rate and velocity during the fast pump-to-turbine process. Notably, the mesh used in this study is not sufficiently fine to resolve all the relevant vortical structures because the computational resources and accuracy must be balanced when simulating the fast pump-to-turbine transition process for more than 100 s. Besides, some of the vortical structures are dampened out by the SST k-ω turbulence model. Therefore, not all the vortical structures were resolved, as shown in Fig. 8.

3.4.3 Analysis of vortex dynamics characteristics

To further understand the hydraulic instability during the fast pump-to-turbine transition process, the Reynolds-averaged transport equation for the enstrophy of rigid vorticity [35] was adopted to analyze the generation and dissipation of vortical structures:

$$\Omega_R = \frac{\omega_R \cdot \omega_R}{2} \tag{6}$$

$$\begin{aligned}&\frac{\partial\left(\bar{\varpi}_{Ri}\cdot\bar{\varpi}_{Ri}/2\right)}{\partial t}+\bar{u}_j\frac{\partial\left(\bar{\varpi}_{Ri}\cdot\bar{\varpi}_{Ri}/2\right)}{\partial x_j}\\ &=\bar{\varpi}_{Rj}\frac{\partial \bar{u}_i}{\partial x_j}\bar{\varpi}_{Ri}+\bar{u}_i\frac{\partial \bar{\varpi}_{Rj}}{\partial x_j}\bar{\varpi}_{Ri}+\left[\left(\frac{\partial \bar{u}_i\bar{\varpi}_{Sj}}{\partial x_j}-\frac{\partial \bar{u}_j\bar{\varpi}_{Si}}{\partial x_j}\right)\bar{\varpi}_{Ri}-\frac{\partial \bar{\varpi}_{Si}}{\partial t}\bar{\varpi}_{Ri}\right]+\nu\frac{\partial^2\bar{\varpi}_i}{\partial x_j\partial x_j}\bar{\varpi}_{Ri}+\nu_{\mathrm{t}}\frac{\partial^2\bar{\varpi}_i}{\partial x_j\partial x_j}\bar{\varpi}_{Ri}\end{aligned} \tag{7}$$

where Ω_R indicates the enstrophy of the rigid vorticity, s^{-2}; $\bar{\varpi}_{Ri}$ (i=1, 2, 3) indicates the Reynolds-averaged rigid vorticity component, s^{-1}; $\bar{\varpi}_{Si}$ (i=1, 2, 3) indicates the Reynolds-averaged shear vorticity component, s^{-1}; $\bar{\varpi}_i$ (i=1, 2, 3) indicates the Reynolds-averaged vorticity component, s^{-1}. In Eq. (7), the left-hand side is the total derivative of the enstrophy of the rigid vorticity, encompassing terms for both the time and convective derivatives. On the right side, the initial term denotes the enstrophy of the rigid vorticity stretching term (ERST), which represents the positive strain intensity of the vortex core line embedding both stretching and compression deformations. The subsequent term, denoted by the enstrophy of the rigid vorticity dilation term (ERDT), captures the shear strain intensity along the vortex core line, accounting for torsional and bending deformations. This term arises from the effect of shear effects on the vortical shape. The third term, known as the enstrophy of the pseudo-lamb vector curl term (ERCT), involves both shear and temporal effects. The fourth term, designated as the enstrophy of the viscous term (ERVT), reflects the inherent dynamic action due to shear processes, representing the diffusion and dissipation strength of vortices induced by fluid viscosity. The fifth term, called the enstrophy of the reynolds stress term (ERRT), captures the diffusion and dissipation strength of vortices induced by turbulent fluctuations. In the context of fluid within a rotating reference frame, an additional term $-2\left(\partial \bar{c}_i \bar{u}_{rj} / \partial x_j - \partial \bar{c}_j \bar{u}_{ri} / \partial x_j\right)\bar{\omega}_{Ri}$, namely the enstrophy of the coriolis force term (ECFT), is introduced and accounts for the influence of inertial effects due to the rotation of vortex evolution, where $\bar{c}_i$ represents the angular velocity component of the rotating system (a constant vector in this study), and $\bar{u}_{ri}$ signifies the velocity component of the fluid relative to the rotating coordinate system.

To quantitatively analyze the distribution and intensity of the Reynolds-averaged enstrophy transport terms for the rigid vorticity in these flow components along the spanwise and streamwise directions, the stay vanes, guide vanes, and runner regions were divided into 20 volumes each along the spanwise direction and 60 volumes in the streamwise direction (each region was divided into 20 volumes). The spanwise volumes were numbered from 0 to 1, moving from the hub to the shroud. The streamwise volumes were numbered from 0 to 1, moving from the inlet to the outlet of the stay vane region; from 1 to 2, moving from the inlet to the outlet of the guide vane region; and from 2 to 3, moving from the inlet to the outlet of the runner region. The schematic of the volume division is shown in Fig. 9. The evolution intensity of the Reynolds-averaged enstrophy for a unit volume E_v is defined by Eq. (7):

$$E_v = \frac{\int \frac{D\Omega_R}{Dt} dV_i}{V_i} \tag{7}$$

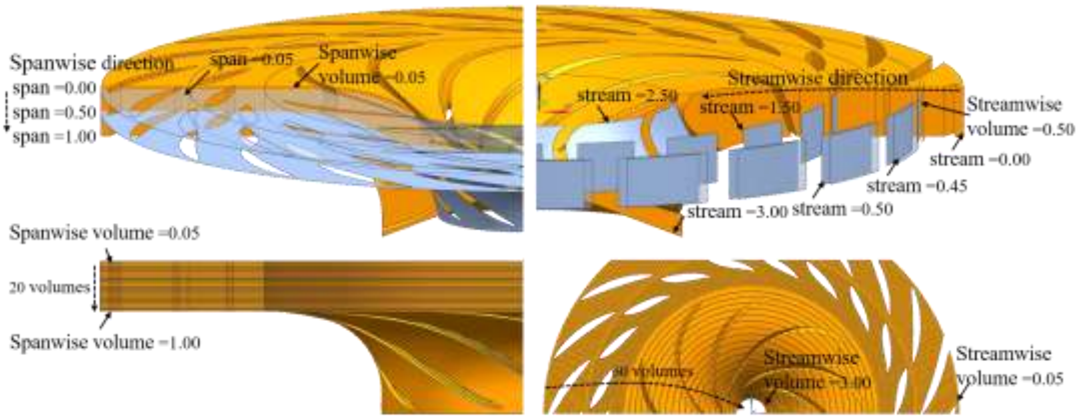

Figure 9. Schematic diagram of the volume division

The distribution and variation of the various transport terms of the Reynolds-averaged enstrophy for a rigid vorticity along the spanwise direction are shown in Fig. 10. It is evident that ERCT plays a key role in the evolution of vortices. From the initial pump operating condition at time t_1 to t_2 when the guide vanes begin to close and the runner speed starts to decrease, and further to t_3 when the flow rate drops to zero, the dissipative effect of the ERCT on the vortices gradually weakens. As the pump turbine transitions into the turbine mode, the ERCT transforms into a vortex generation effect. However, with the phased opening of the guide vanes, the vortex generation effect of the ERCT gradually diminished until it entered the turbine no-load operating condition. Subsequently, the ECFT becomes the primary driver in the evolution of the vortices owing to the small opening of the guide vanes and the unloaded pump-turbine unit. This is primarily manifested by the rotation of the blade, which generates vortices within the flow passage. Additionally, the intensity of the ERDT increased near the hub and shroud, making the vortical structures prone to twisting deformation.

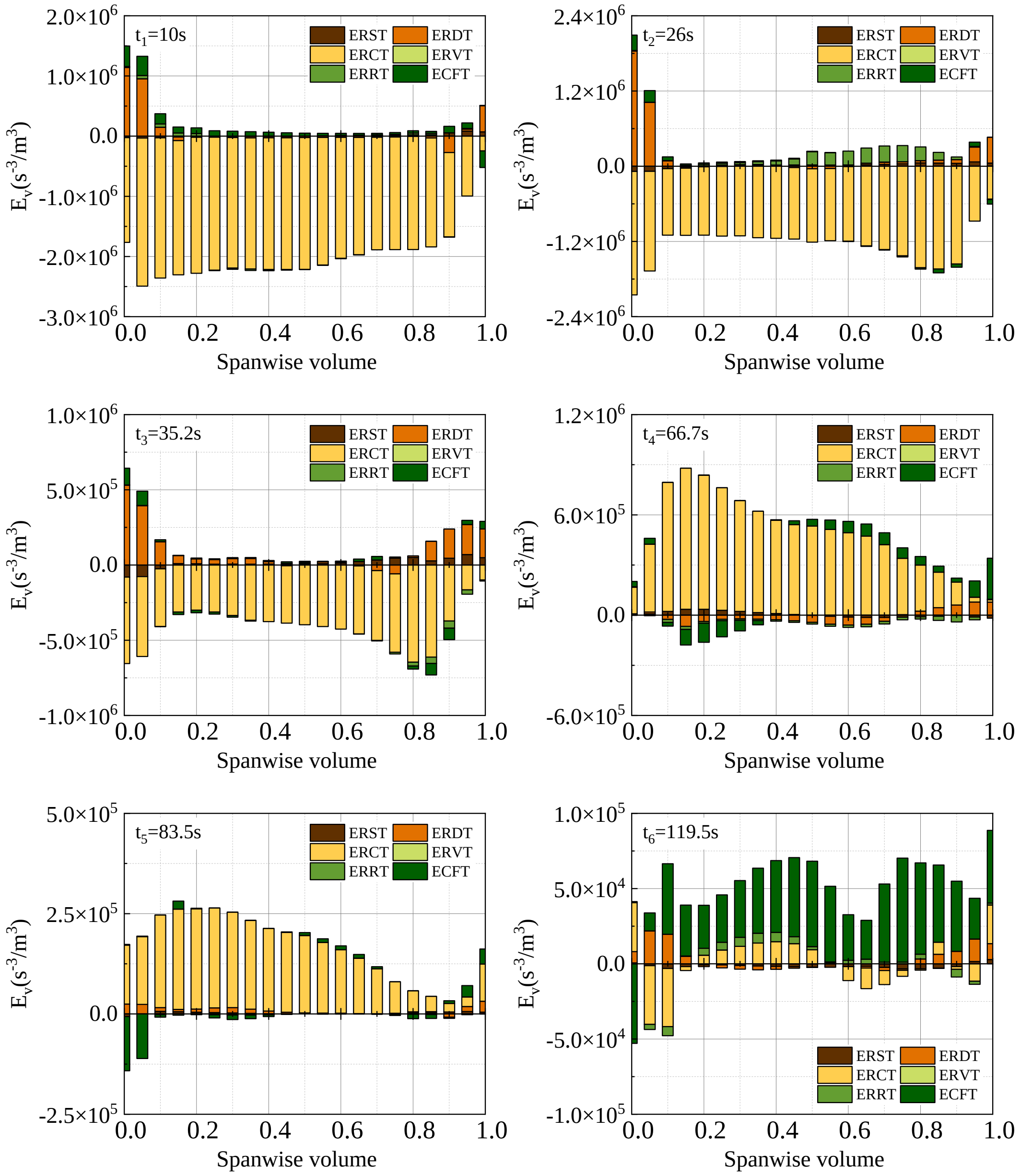

Figure 10. The distribution and intensity of E_v variation along the spanwise direction

The distribution and variation of the various transport terms of the Reynolds-averaged enstrophy for a rigid vorticity along the streamwise direction are shown in Fig. 11. Consistent with the distribution and variation in the spanwise direction, the ERCT remains the primary factor influencing the evolution of vortices in the streamwise direction. In the turbine no-load operating condition, the ECFT replaces the ERCT as the predominant factor governing vortex evolution in the streamwise direction. The significant variation in the ECFT between the runner inlet and outlet intensified and led to the formation of vortical structures at these locations (see Fig. 8). The magnitude of E_v is notably larger in the streamwise volume range of 2 to 3, indicating that the transport terms of the Reynolds-averaged enstrophy for the rigid vorticity within the runner domain exert a stronger influence on the evolution of vortical structures than the stay and guide vane regions. Moreover, in pump mode, the ERDT affects the entire streamwise direction within the runner domain, thus resulting in a twisting deformation of the vortical structures along the streamwise direction.

In the stay and guide vane regions, vortical structures are prone to occur in the middle of the guide vane passages, specifically around a streamwise volume of 1.5. This result is consistent with the vortex identification results presented in Fig. 8. In the stay-vane region, vortical structures primarily appeared near the leading and trailing edges of the blades.

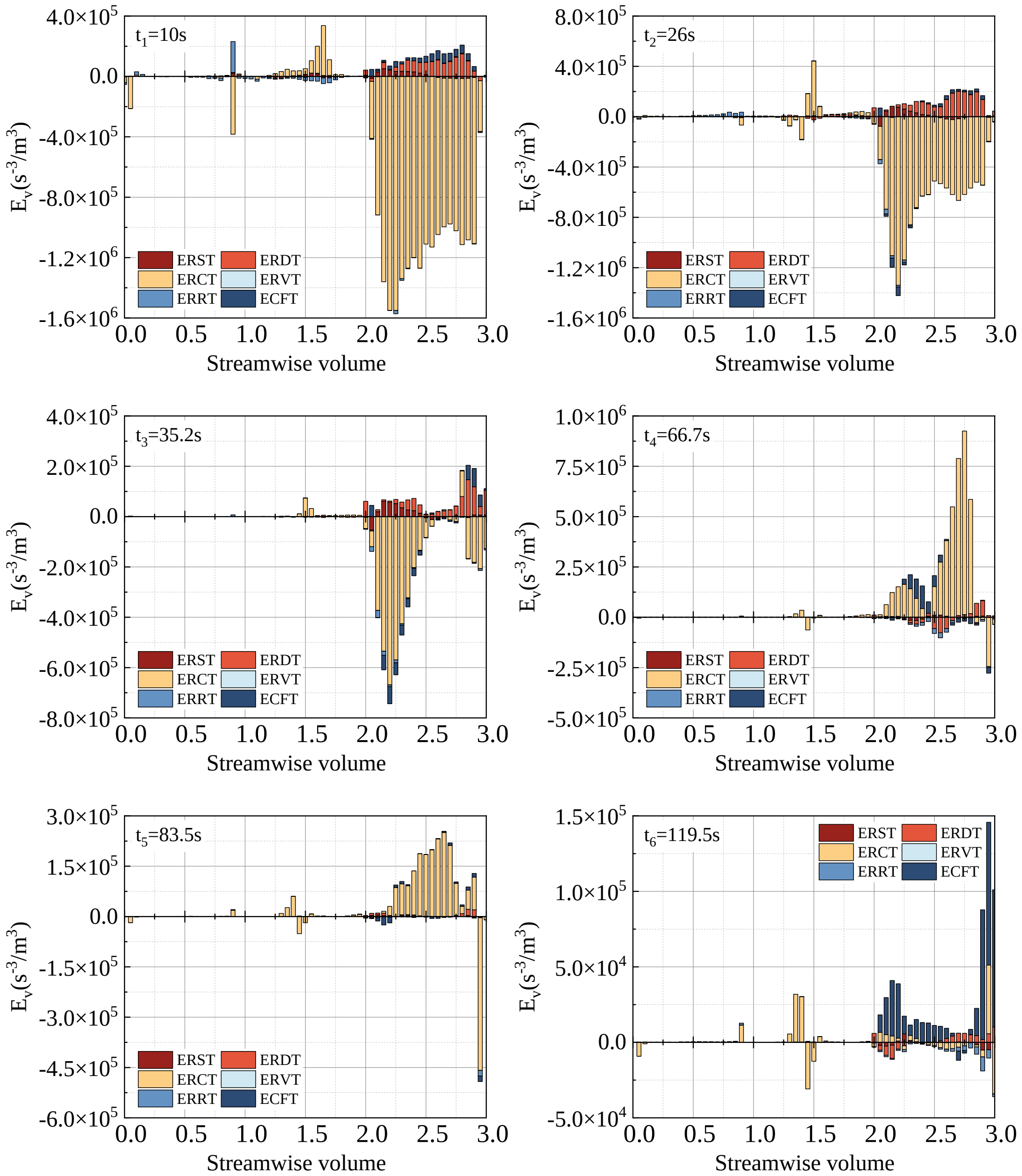

Figure 11. The distribution and intensity of E_v variation along the streamwise direction

3.4.4 Evolution of flow patterns and vortical structures

To provide further evidence of the flow pattern evolution and vortices in the fast pump-to-turbine process in pumped storage, the distributions of pressure, velocity, rigid vorticity, and ERCT, which play primary roles in the evolution of vortices, are depicted at six characteristic moments (see Fig. 12).

At the initial moment t_1, the pump-turbine unit operates in pump mode, pumping water from the runner into the guide vanes. Owing to this impact, vortices appeared at the leading edge of the guide vanes. High ERCT values were primarily distributed in regions near the leading edges of the guide and stay vanes as well as on the suction side of the runner blades. The pressure distribution within the runner blades increases uniformly from the runner to the spiral casing.

At t_2, the guide vanes are fully closed, and the runner speed starts to decrease. Owing to inertia, the runner continues to rotate and pumps water out. However, obstruction due to closed guide vanes causes a rapid pressure increase in the vaneless region, generating high-speed circulation. The flow in the stay vanes and spiral casing domain started to become chaotic, vortical structures emerged near the runner blade suction side, and the guide vanes were cleared.

At t_3, the flow rate drops to zero, and both the pressure and high-speed circulation in the vaneless region decrease owing to decreases in the speed and flow rate. The flow in the stay vanes and spiral casing domain became increasingly chaotic, and regions with high ERCT values and vortical structures appeared near the runner blade pressure side.

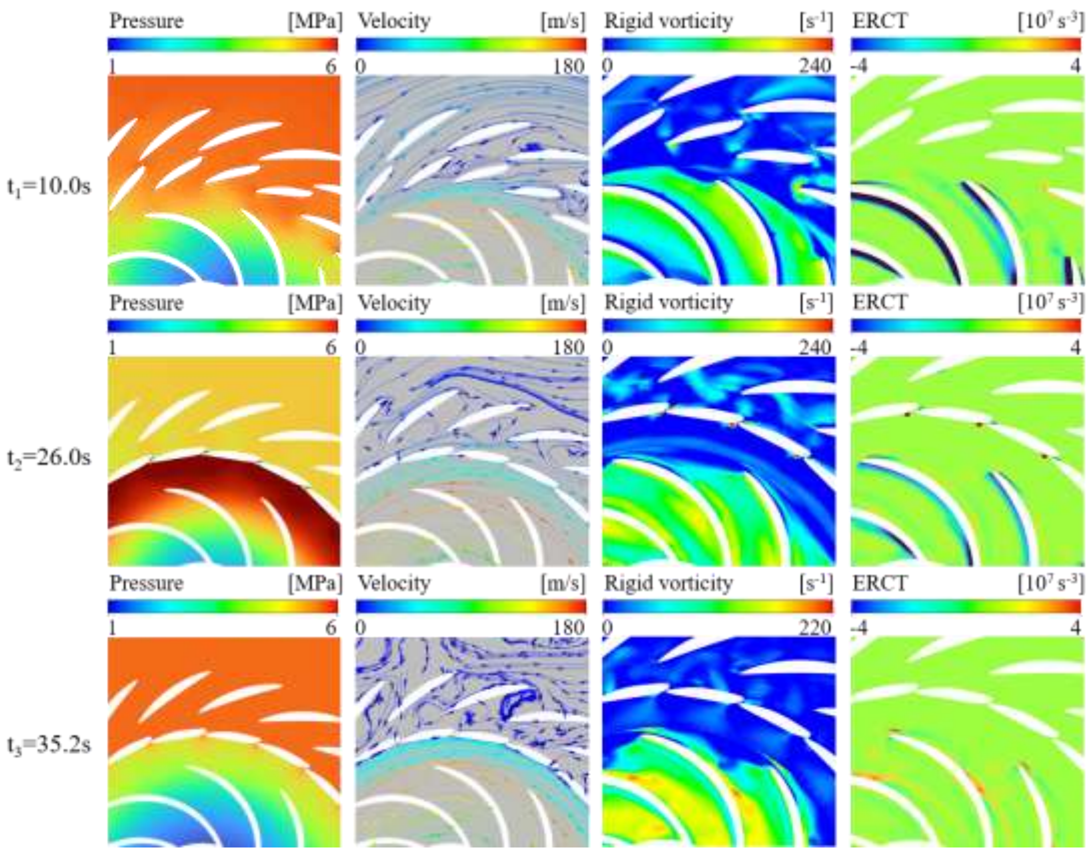

Figure 12 (a). Evolution of the flow patterns and vortical structures at time t_1, t_2, and t_3

From t_3 to t_4, the pressure within the runner region decreased continuously as the speed continued to decrease. From t_4 to t_6, the runner changed its rotational direction to the turbine mode, and the pump-turbine unit entered the turbine mode. As the guide vanes gradually opened, the pressure gradient within the flow domain gradually became more uniform, and the intensity of high-speed circulation in the vaneless region decreased.

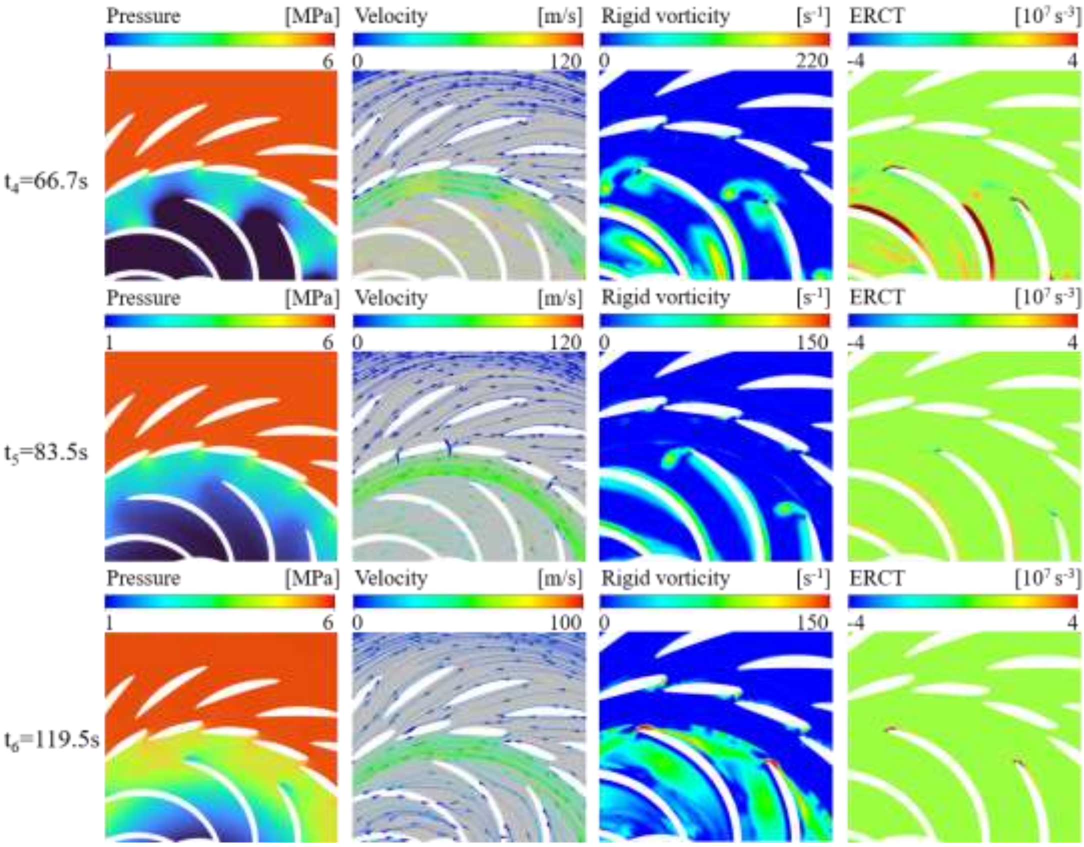

Figure 12 (b). Evolution of the flow patterns and vortical structures at time t_4, t_5, and t_6

4 Conclusions

This paper reports a numerical three-dimensional model of the entire flow system of a pumped storage station. Simulations were performed to investigate fast pump-to-turbine transition processes. This research delved into the variations in external parameters, pressure fluctuations within the pump-turbine unit, and the evolution of flow patterns and vortical structures during the fast pump-to-turbine transition process. To the authors' opinion, this research considerably contributes to the understanding of the hydraulic transient mechanisms during the fast pump-to-turbine transition process and provides theoretical guidance for enhancing stability and optimizing control strategies during the transitional process. In particular:

1) During the fast pump-to-turbine transition process, the opening and closing of the guide vanes instantaneously impact the hydrodynamic performance within the pump-turbine unit. Variations in the flow rate, torque, and axial force exhibited stepwise changes during the movement of the guide vanes. Periods of significant oscillation and drastic fluctuations in torque are prone to occur during pump braking and reversal of runner speed.
2) Under the influence of vortical structures at different scales and intensities, the pressure fluctuations within the vaneless region and runner exhibit significant variations during the transition process. Notably, the pressure fluctuations in the vaneless region were particularly pronounced. The temporal variations in pressure at the monitoring points in the spiral casing, stay vanes, and guide vane regions

exhibit similar trends, with the magnitude of pressure variations increasing from the spiral casing to the guide vanes. The draft tube region did not generate a tailrace eddy, thereby avoiding intense pressure fluctuations.

3) During the fast pump-to-turbine transition process, the inertia of the water flow and the blocking effect of the guide vanes contributed to the occurrence of high-speed circulation in the vaneless region, which was the reason for the intense pressure fluctuations observed in the vaneless region. The internal flow was radically altered and became more complex when the guide vanes were closed, the flow rate approached zero, or the runner speed decreased to zero. Rapid changes in the guide vane opening, flow direction, and rotational direction were the main causes of hydraulic instability of the pump turbine.

Building on the foundation laid in this study, future investigations can delve deeper into the hydraulic transient mechanisms during the critical phases of the transition process. Furthermore, exploring the impact of various guide vane control strategies on this transition process and optimizing these control strategies represents another avenue for future research.

Acknowledgments

This work was supported by the National Natural Science Foundation of China (52379086, 52271275), the Jiangsu Innovation Support Programme for International Science and Technology Cooperation (BZ2023047), and the Postdoctoral Research Foundation of China (2022T150185; 2022M711021). The computational work was supported by the High-Performance Computing Platform at Hohai University. The support of Hohai University is also gratefully acknowledged.

References

[1] Erdogan S, Pata UK, Solarin SA. Towards carbon-neutral world: The effect of renewable energy investments and technologies in G7 countries. Renewable and Sustainable Energy Reviews. 2023;186:113683.

[2] Li P, Zhao Z, Li J, Liu Z, Liu Y, Mahmud MA, et al. Unlocking potential contribution of seasonal pumped storage to ensure the flexibility of power systems with high proportion of renewable energy sources. Renewable Energy. 2023;218:119280.

[3] Li D, Zuo Z, Wang H, Liu S, Wei X, Qin D. Review of positive slopes on pump performance characteristics of pump-turbines. Renewable and Sustainable Energy Reviews. 2019;112:901-16.

[4] Zuo Z, Liu S. Flow-induced instabilities in pump-turbines in China. Engineering. 2017;3(4):504-11.

[5] Xu L, Liu D, Li Z, Zhao X, Liu X. Experimental and numerical simulation research on flow characteristics of model pump-turbine in four-quadrant operating quadrants. Journal of Energy Storage. 2022;54:105083.

[6] Wang W, Guo H, Zhang C, Shen J, Pei J, Yuan S. Transient characteristics of PAT in micro pumped hydro energy storage during abnormal shutdown process. Renewable Energy. 2023;209:401-12.

[7] Liu D, Li Z, Xu L, Li J, Yang Y, Wang X, et al. Vortex motion in vaneless space and runner passage of pump-turbine in S-shaped region. Physics of Fluids. 2024;36(2).

[8] Liu J, Liu S, Sun Y, Jiao L, Wu Y, Wang L. Three-dimensional flow simulation of transient power interruption process of a prototype pump-turbine at pump mode. Journal of Mechanical Science and Technology. 2013;27:1305-12.

[9] Li Z, Bi H, Karney B, Wang Z, Yao Z. Three-dimensional transient simulation of a prototype pump-

turbine during normal turbine shutdown. Journal of Hydraulic Research. 2017;55(4):520-37.

[10] Zhang H, Chen D, Wu C, Wang X, Lee J-M, Jung K-H. Dynamic modeling and dynamical analysis of pump-turbines in S-shaped regions during runaway operation. Energy Conversion and Management. 2017;138:375-82.

[11] Mao X, Chen X, Lu J, Liu P, Zhang Z. Improving internal fluid stability of pump turbine in load rejection process by co-adjusting inlet valve and guide vane. Journal of Energy Storage. 2022;50:104623.

[12] Jin F, Wang H, Luo Y, Presas A, Bi H, Wang Z, et al. Visualization research of energy dissipation in a pump turbine unit during turbine mode's starting up. Renewable Energy. 2023;217:119172.

[13] Zhang F, Zheng Y, Zhao Y, Wang K. Pumped-storage Unit Stability Comparison of Pumping Operation to Generating Operation in Different Mode. Journal of Vibration Engineering. 2024;37(1): 104-112. (in Chinese)

[14] Zhang H, Su D, Guo P, Zhang B, Mao Z. Stochastic dynamic modeling and simulation of a pump-turbine in load-rejection process. Journal of Energy Storage. 2021;35:102196.

[15] Wang W, Guo H, Zhang C, Shen J, Pei J, Yuan S. Transient characteristics of PAT in micro pumped hydro energy storage during abnormal shutdown process. Renewable Energy. 2023;209:401-12.

[16] Jin F, Luo Y, Bi H, Wang H, Wang Z, Lin K, et al. Transient simulation of reversible pump turbine during pump mode's starting up. Journal of Energy Storage. 2023;68:107678.

[17] Yang Z, Liu Z, Cheng Y, Zhang X, Liu K, Xia L. Differences of flow patterns and pressure pulsations in four prototype pump-turbines during runaway transient processes. Energies. 2020;13(20):5269.

[18] Liu F, Li Z, Liang M, Zhao B, Ding J. Prediction method of non-stationary random vibration fatigue reliability of turbine runner blade based on transfer learning. Reliability Engineering & System Safety. 2023;235:109215.

[19] Han Y, Tan L. Influence of rotating speed on tip leakage vortex in a mixed flow pump as turbine at pump mode. Renewable Energy. 2020;162:144-50.

[20] Kan K, Chen H, Zheng Y, Zhou D, Binama M, Dai J. Transient characteristics during power-off process in a shaft extension tubular pump by using a suitable numerical model. Renewable Energy. 2021;164:109–121.

[21] Jin F, Tao R, Zhu D, Li P, Xiao R, Liu W. Transient simulation of the rapid guide vane adjustment under constant head of pump turbine in pump mode. Journal of Energy Storage. 2022;56:105960.

[22] Roy CJ. Grid convergence error analysis for mixed-order numerical schemes. AIAA journal. 2003;41(4):595-604.

[23] Kan K, Zhao F, Xu H, Feng J, Chen H, Liu W. Energy performance evaluation of an axial-flow pump as turbine under conventional and reverse operating modes based on an energy loss intensity model. Physics of Fluids, 2023, 35(1).

[24] Kan K, Yang Z, Lyu P, Zheng Y, Shen, L. Numerical study of turbulent flow past a rotating axial-flow pump based on a level-set immersed boundary method. Renewable Energy. 2021;168:960–971.

[25] Stern F, Wilson RV, Coleman HW, Paterson EG. Comprehensive approach to verification and validation of CFD simulations—part 1: methodology and procedures. J Fluids Eng. 2001;123(4):793-802.

[26] Celik IB, Ghia U, Roache PJ, Freitas CJ. Procedure for estimation and reporting of uncertainty due to discretization in CFD applications. Journal of fluids Engineering-Transactions of the ASME. 2008;130(7).

[27] Wilson RV, Stern F, Coleman HW, Paterson EG. Comprehensive approach to verification and

validation of CFD simulations—Part 2: Application for RANS simulation of a cargo/container ship. J Fluids Eng. 2001;123(4):803-10.

[28] Jiang D. Vorticity decomposition and its application to sectional flow characterization. Tectonophysics. 1999;301(3-4):243-59.

[29] Liu J, Gao Y, Liu C. An objective version of the Rortex vector for vortex identification. Physics of Fluids. 2019;31(6).

[30] Gao Y, Liu C. Rortex based velocity gradient tensor decomposition. Physics of Fluids. 2019;31(1).

[31] Wang Y, Gao Y, Liu J, Liu C. Explicit formula for the Liutex vector and physical meaning of vorticity based on the Liutex-Shear decomposition. Journal of Hydrodynamics. 2019;31:464-74.

[32] Dong X, Hao C, Liu C. Correlation between vorticity, Liutex and shear in boundary layer transition. Computers & Fluids. 2022;238:105371.

[33] Wang D, Liu Y, Li H, Xu H. Secondary instability of channel-confined transition around dual-circular cylinders in tandem. International Journal of Mechanical Sciences. 2021;208:106692.

[34] Zhang Z, Dong S, Jin R, Dong K, Wang B. Vortex characteristics of a gas cyclone determined with different vortex identification methods. Powder Technology. 2022;404:117370.

[35] Yan X, Kan K, Zheng Y, Xu Z, Rossi M, Xu L, et al. The vortex dynamics characteristics in a pump-turbine: A rigid vorticity analysis while varying guide vane openings in turbine mode. Energy. 2024;289:130086.

[36] Chen S, Yang L, Zhao W, Wan D. Wall-modeled large eddy simulation for the flows around an axisymmetric body of revolution. Journal of Hydrodynamics. 2023:1-11.

[37] Bai X, Cheng H, Ji B, Long X, Qian Z, Peng X. Comparative study of different vortex identification methods in a tip-leakage cavitating flow. Ocean Engineering. 2020;207:107373.